Unlocking hidden spins in centrosymmetric 1*T* transition metal dichalcogenides by vacancy-controlled spin-orbit scattering

Hengzhe Lu,[1,*] Zhibin Qi,[1,*] Yuqiang Huang,[1,*] Man Cheng,[1,*] Feng Sheng,[1] Zhengkuan Deng,[1] Shi Chen,[2] Chenqiang Hua,[3] Pimo He,[1] Yunhao Lu,[1] and Yi Zheng[1,4,†]

[1]*Zhejiang Province Key Laboratory of Quantum Technology and Device, School of Physics, and State Key Laboratory of Silicon Materials, Zhejiang University, Hangzhou 310027, China*

[2]*Institute of Applied Physics and Materials Engineering, University of Macau, Macao, China*

[3]*Beihang Hangzhou Innovation Institute Yuhang, Hangzhou 310023, China*

[4]*Collaborative Innovation Centre of Advanced Microstructures, Nanjing University, Nanjing 210093, China*

(Received 31 August 2022; revised 7 April 2023; accepted 11 April 2023; published 25 April 2023)

Spin current generation and manipulation remain the key challenge of spintronics, in which relativistic spin-orbit coupling (SOC) plays a ubiquitous role. In this paper, we demonstrate that hidden Rashba spins in the nonmagnetic, centrosymmetric lattice of multilayer $SnSe_2$ can be efficiently activated by spin-orbit scattering introduced by Se vacancies. Via vacancy scattering, conduction electrons with hidden spin-momentum locked polarizations acquire out-of-plane magnetization components, which effectively break the chiral symmetry between the two Se sublattices of an $SnSe_2$ monolayer when electron spins start precession in the strong built-in Rashba SOC field. The resulting spin separations are manifested in quantum transport as vacancy concentration- and temperature-dependent crossovers from weak antilocalization to weak localization, with the distinctive spin relaxation mechanism of the D'yakonov-Perel' type. In a nonlocal geometry, the generated spins exhibit a long diffusion length exceeding 5 μm, when fast momentum scattering protects the effective spin polarizations by driving the random-walk evolution of spin precessions subject to rapidly changing Rashba SOC field. Our study shows the great potential of two-dimensional systems with hidden-spin textures for spintronics.

DOI: 10.1103/PhysRevB.107.165419

I. INTRODUCTION

For a nonmagnetic centrosymmetric bulk system, relativistic spin-orbit coupling (SOC) effects are quenched due to the coexistence of both time-reversal and inversion symmetries, which enforce spin double degeneracy for all electronic bands [1–4]. However, recent theoretical works reveal that many crystal systems host hidden spin polarization introduced by atomic-site inversion asymmetries, viz., local dipole field (corresponding to R2-Rashba SOC) and site inversion asymmetry (D2-Dresselhaus SOC), respectively [5–7]. Hidden-spin textures, in particular R2-Rashba SOC, become an eminent feature in various van der Waals (vdW) crystals with the 1*T*-type transition metal dichalcogenide (TMDC) monolayer structure, in which two opposite spin-momentum locked polarization directions within the vdW plane manifest the local dipole field asymmetry exerted on the two inversion-symmetric chalcogen sublattices [8,9]. Recently, many research efforts have been focused on the main-group IV–VI dichalcogenides GeS_2, SnS_2, and $SnSe_2$, aiming for diverse device applications ranging from thermoelectric [10] and optoelectronic [11] to composite photocatalyzing [12]. Noticeably, the doubly degenerate electronic bands of these vdW semiconductors are also spin polarized by the innate strong R2-Rashba SOC, rooted in the 1*T*-TMDC monolayer lattice.

From a spintronics point of view, these emergent two-dimensional (2D) materials are promising spin transport channels for the next-generation spin logics and field-effect transistors (FETs) [13,14], considering that the inherent SOC of these systems is an order-of-magnitude larger than that of the intensively explored graphene [15]. However, spin transport and spin relaxation studies focusing on heavy-element 2D systems remain scarce at the moment [15,16]. Most critically, for hidden-spin crystals, it seems to be formidable to achieve long spin diffusion lengths and long spin relaxation times, since there is a minimal energy cost for a conduction electron to hop between two sublattices by flipping the spin polarization directions.

In this paper, we show that counterintuitively, spin transport and relaxation in the centrosymmetric lattice of multilayer $SnSe_2$ are not limited by random spin flipping, but rather tailored by *motional narrowing* associated with the D'yakonov-Perel' (DP) mechanism, when fast momentum relaxation facilitates the random walking of electron spin precessions in the strong built-in R2-Rashba SOC field. The activation of the hidden Rashba spins is realized by spin-orbit scattering induced by Se vacancies, which enable conduction electrons to acquire out-of-plane magnetization components and thus effectively break the chiral symmetry between the two Se sublattices. The resulting spin polarizations are manifested in quantum transport as vacancy concentration- and

*These authors contributed equally to this work.
†phyzhengyi@zju.edu.cn

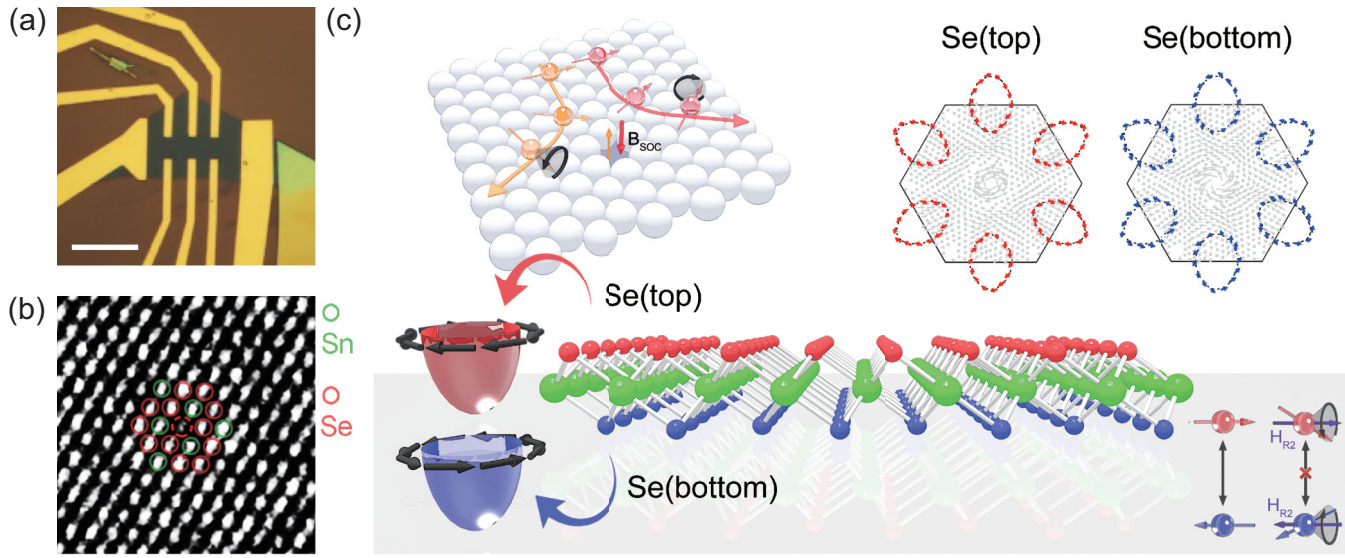

FIG. 1. Unlocking hidden Rashba spins in 1T-$SnSe_2$ by SOC scattering. (a) Optical image of a multilayer $SnSe_2$ device. Scale bar, 15 μm. (b) HRTEM image of few-layer $SnSe_2$, in which a single Se vacancy in darker contrast is highlighted by the red dashed circle. (c) Vacancy-induced SOC scattering and the unlocking of hidden R2-Rashba spins in 1T-$SnSe_2$. Upper left: SOC scattering by a negatively charged Se vacancy introduces effective SOC fields $\mathbf{B}_{SOC}$ with opposite signs for left- and right-side scattered electrons, respectively, i.e., the extrinsic SHE. Upper right: DFT-calculated in-plane spin projection (gray arrows) of the first conduction band in the first Brillouin zone. The red and blue arrows are the hidden-spin textures of FSs with $n = 1 \times 10^{14}$ cm^{-2}. Note that the experimental FSs of $\sim 10^{13}$ cm^{-2} are too small for illustration. Bottom: sublattice-indexed chiral symmetry of 1T-$SnSe_2$. Spin precessions break the chiral symmetry and prohibit intersublattice hopping.

temperature-dependent crossovers from weak antilocalization (WAL) to weak localization (WL), which are excellently fitted by the Iordanskii–Lyanda-Geller–Pikus (ILP) theory. Using nonlocal measurements, we demonstrate that the spin-orbit-scattering-induced effective spin polarizations have a long diffusion length exceeding 5 μm, providing unambiguous evidence of the activation of hidden Rashba spins.

II. VACANCIES INDUCED SPIN-ORBIT SCATTERING

$SnSe_2$ single crystals with controllable Se-vacancy concentrations are synthesized by the self-flux method [17]. Standard micromechanical exfoliations readily yield thin $SnSe_2$ flakes, as shown in the Supplemental Material [18] (see also Refs. [17,19–23] therein) for a representative sample with consecutive thicknesses from monolayer to sextuple-layer [24]. All transport-measuring $SnSe_2$ devices [one representative optical image is shown in Fig. 1(a)] have been further characterized by Raman spectroscopy to confirm the trigonal lattice structures, which have the fingerprinting E_g and A_{1g} phonon modes [17]. Using high-resolution transmission electron microscopy (HRTEM), we confirm the existence of randomly distributed Se single vacancies with a moderate density of $\sim 10^{11}$ cm^{-2} [Fig. 1(b)], corresponding to electron doping of $n \sim 10^{12}$ cm^{-2} based on density functional theory (DFT) calculations [18]. In brief, the vacancy concentrations can be controlled by the growth temperature T with a fixed Sn-to-Se stoichiometric ratio of 1 : 2 [17]. Typically, a growth T of about 600 °C will lead to $SnSe_2$ crystals containing Se vacancies comparable to those in Fig. 1(b). By lowering T, the vacancy densities of $SnSe_2$ crystals decrease accordingly, which become negligible for crystals synthesized at around 400 °C. Since multilayer and few-layer microflakes may show significant variations from the bulk crystals, we use Hall measurements for calibrating the sample-dependent vacancy densities. Multilayer $SnSe_2$ FETs with typical channel thicknesses of ∼10 nm for quantum transport were prepared by electron beam lithography followed by thermal evaporation of metal electrodes (5 nm Ti and 50 nm Au). The devices were then measured in a variable-temperature Oxford 14-T system using the standard four-probe technique with lock-in amplifiers.

As illustrated in the upper left panel of Fig. 1(c), the presence of negatively charged Se vacancies [18] causes strong SOC scattering for conduction electrons to acquire out-of-plane magnetization components, which is essentially the spin Hall effect (SHE) [25]. Although similar extrinsic SHE phenomena have been reported in surface hydrogenated graphene [26], the inherent strong R2-Rashba SOC makes a fundamental difference in the spin relaxation mechanism of multilayer $SnSe_2$. Without vacancy-site SOC scattering, electron spins are in-plane polarized along two opposite spin-momentum locking directions with the same energy, as shown by the DFT-calculated hidden-spin textures in the upper right panel of Fig. 1(c) [18]. Like pseudospins in graphene, the clockwise (counterclockwise) spin-momentum locking relation describes the instantaneous location of an electron spin wave function in the Se-top (Se-bottom) atomic layer of an $SnSe_2$ monolayer, i.e., the sublattice-indexed chiral symmetry. Due to the energy degeneracy, conduction electrons are constantly hopping between two Se sublattices by flipping the spin polarizations, suggesting long spin diffusion lengths and long spin relaxation times unrealistic for a hidden-spin system such as $SnSe_2$. However, once they acquire an out-of-plane

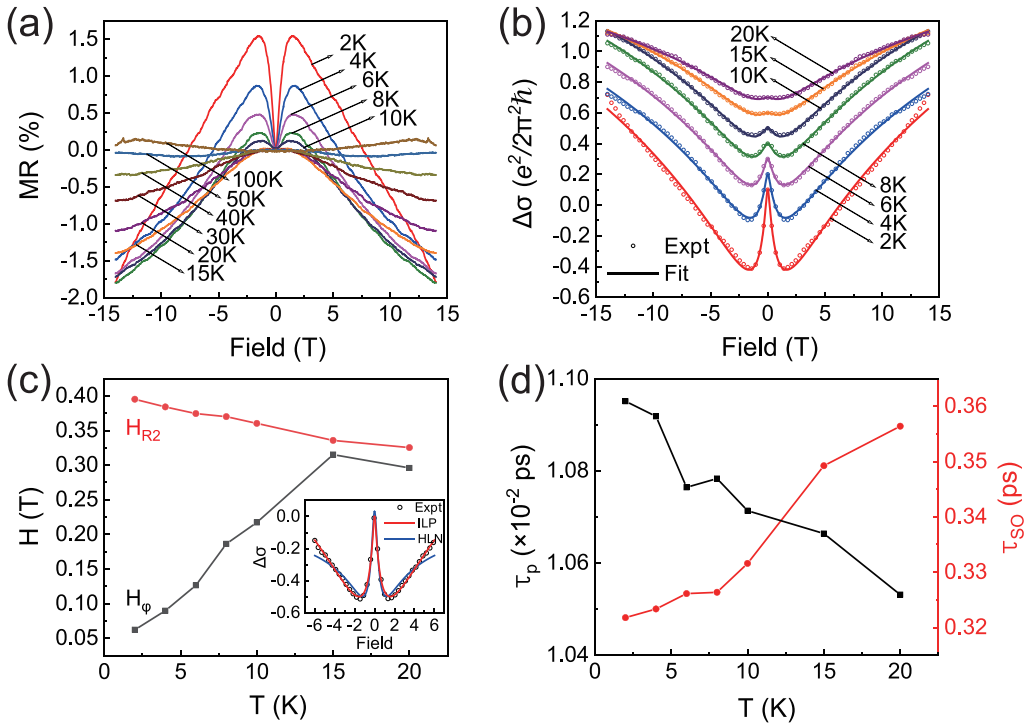

FIG. 2. Quantum signatures of the hidden-spin activation in multilayer $SnSe_2$. (a) T-dependent MR characteristics of $SnSe_2$ FET device SS5, showing distinctive WAL-to-WL transitions. (b) The corresponding MC curves, fitted by the ILP theory. Each MC curve is offset to show the remarkable consistency between the experimental results and the ILP model. (c) H_φ and H_{R2} extracted from the ILP fitting. Inset: the fitting results of the ILP theory compared with the HLN model. (d) τ_{SO} extracted from the ILP theory fitting, showing an inverse relation of $\tau_{SO} \propto \tau_p^{-1}$, hallmarking the DP mechanism.

magnetization, SOC scattered electrons start spin precession as driven by the strong built-in Rashba SOC field (H_{R2}). As shown in the bottom panel of Fig. 1(c), the spin precession effectively breaks the chiral symmetry between the two Se atomic layers, because intersublattice electron hopping now must enforce a reversal in the spin precession directions as required by the flipping of H_{R2}.

Intriguingly, by unlocking hidden Rashba spins using Se-vacancy scattering, spin polarizations obtain a finite relaxation time τ_{SO} dependent on the competition between the spin precession time $T_1 \propto 1/H_{R2}$ and momentum scattering time τ_p, which can be quantitatively probed by T-dependent quantum transport measurements [16,27–29]. As shown in Fig. 2(a) for a representative device (FET device SS5), helium temperature charge transport of multilayer $SnSe_2$ FETs is characterized by pronounced crossover behaviors from low-field WAL to high-field WL, hallmarking quantum interference corrections of spin-polarized electron wave functions to the mesoscopic current flow [27,30–33]. By gradually warming up the sample, it is evident that the WAL phenomena are vanishing at 15 K, while the WL-contributed negative magnetoresistance (MR) persists up to $T = 40$ K. By plotting the data onto the magnetoconductivity (MC) curves, we can clearly see the dwindling of the characteristic WAL cusps as a function of T, which can be fitted excellently by the ILP theory [34],

$$\Delta\sigma(B_\perp) = \frac{e^2}{2\pi^2\hbar}\left\{\Psi\left(\frac{1}{2}+\frac{H_\varphi}{B_\perp}+\frac{H_{R2}}{B_\perp}\right)+\frac{1}{2}\Psi\left(\frac{1}{2}+\frac{H_\varphi}{B_\perp}+2\frac{H_{R2}}{B_\perp}\right)-\frac{1}{2}\Psi\left(\frac{1}{2}+\frac{H_\varphi}{B_\perp}\right)\right.$$
$$\left.-\ln\left(\frac{H_\varphi}{B_\perp}+\frac{H_{R2}}{B_\perp}\right)-\frac{1}{2}\ln\left(\frac{H_\varphi}{B_\perp}+2\frac{H_{R2}}{B_\perp}\right)+\frac{1}{2}\ln\left(\frac{H_\varphi}{B_\perp}\right)\right\}, \quad (1)$$

in which Ψ is the digamma function, H_φ is the characteristic field of phase coherence [35], and $B_\perp$ represents the external magnetic field. As shown in Fig. 2(b), the ILP formula not only reproduces the low-field WAL cusps but also captures the $B_\perp$-dependent WAL-to-WL crossover with remarkable consistency. In the seminal works of D'yakonov and Perel' [36] and Pikus and co-workers [37], it has been elucidated that the applicability of the ILP theory is a manifestation of the DP spin relaxation mechanism. In contrast, for an inversion-symmetric system, WAL of spin degenerate electron wave functions should be activated by the Elliot-Yafet mechanism with $\tau_{SO} \propto \tau_p$, modeled by the Hikami-Larkin-Nagaoka (HLN) theory [38–40]. As compared in the inset of Fig. 2(c), the HLN model can fairly fit the low-field WAL with

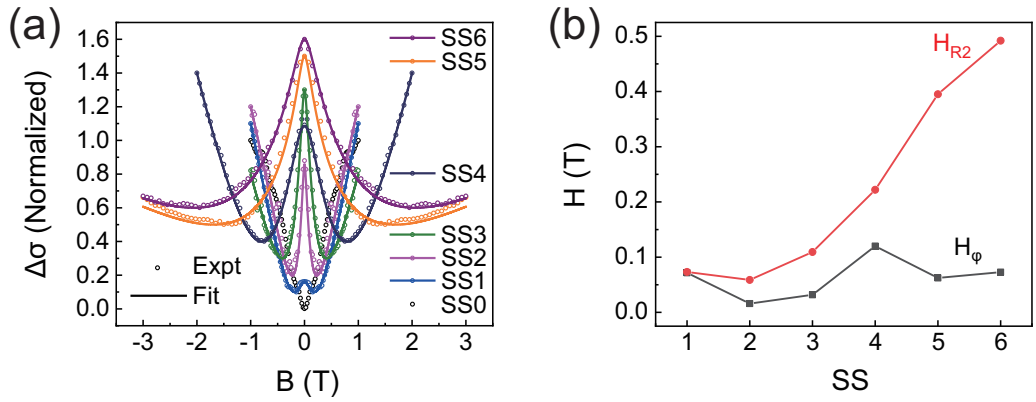

FIG. 3. Se-vacancy-concentration-controlled WAL-to-WL crossovers and effective spin polarizations in $SnSe_2$. (a) MC curves of seven multilayer $SnSe_2$ FETs (designated as FET devices SS0–SS6, respectively) at $T = 2$ K with increasing electron doping, which are proportional to the Se-vacancy densities. Note that FET device SS0 has negligible Se vacancies. The different curves are normalized by the zero-field maximum and offset for clarity. (b) H_φ and H_{SO} extracted from the ILP theory fitting. By increasing Se-vacancy densities, enhanced SOC scattering makes conduction electrons more effectively spin polarized, leading to the monotonic growth in H_{R2}.

an overshooting zero-field peak; however, it fails completely to conform to the crossover regime and the succeeding WL growth.

Using the ILP theory fitting, we are able to extract the T-dependent H_φ and H_{R2}. As shown in Fig. 2(c), below 15 K, H_{R2} is much larger than H_φ, which explains the robust WAL behaviors in this T regime. Noticeably, H_{R2} exhibits a very weak T dependence, which is expected for a built-in R2-Rashba SOC field. In contrast, H_φ monotonically increases as a function of T, due to enhanced inelastic scattering at elevated T. The different T dependence of H_{R2} and H_φ is responsible for the dwindling of the WAL cusps. Equally important, the ILP theory is microscopically originating in the DP spin relaxation mechanism, which correlates τ_{SO} inversely to τ_p by *motional narrowing* [14,26], i.e., frequent momentum scattering interrupts the full spin precession cycles and causes random walking in spin dephasing. For Se-vacancy scattered conduction electrons in $SnSe_2$, motional narrowing effectively increases the lifetime of the SOC-induced out-of-plane magnetization, during which inter-Se-sublattice hopping costs finite energy to reverse the spin precession directions. By extracting τ_p using the Drude model [41], we can indeed see the inverse relation of $\tau_{SO} \propto \tau_p^{-1}$, as shown in Fig. 2(d).

The critical role of Se-vacancy scattering in the activation of hidden Rashba spins is also demonstrated by a positive dependence of H_{R2} on electron doping n, which is directly controlled by vacancy densities. As compared in Figs. 3 and S5 [18] for seven different FETs (designated as FET devices SS0–SS6), with the presence of more Se vacancies, the conduction electrons have increased SOC scattering rates, causing them to acquire out-of-plane magnetization components, and thus H_{R2} monotonically grows while H_φ remains nearly unchanged. By defining the WAL minima as H_{WAL}, which also reflects the magnitude of H_{R2}, it is also clear that the presence of increased Se vacancies contributes positively to spin polarizations and τ_{SO} in $SnSe_2$ [18].

It should be noticed that Eq. (1) is a reduced form of the original ILP theory, with the prerequisite of the **k**-cubic Rashba terms ($H_{R2}^{(3)}$) being predominant over the **k**-linear Rashba SOC ($H_{R2}^{(1)}$) [42,43]. Explicitly, H_{R2} should be expressed as $H_{R2} = H_{R2}^{(1)} + H_{R2}^{(3)}$, in which $H_{R2}^{(3)}$ is sensitive to the Fermi surface (FS) positions due to its cubic dependence on **k** [44]. The leading contribution of $H_{R2}^{(3)}$ to the WAL-to-WL transitions is verified by a study of MR dependent on gate voltage V_g, which dynamically reveals the evolutions of WAL-to-WL crossovers as a function of FS positions. Figures 4(a)–4(d) summarize the V_g-dependent transport results of FET device SS3 within the range ±50 V. For positive V_g, which enlarges the FS areas by introducing more electron doping, the ILP theory analyses indeed reveal a linear decrease in τ_{SO}, accompanied by the inverse growth of τ_p. In contrast, for negative V_g, the inverse relation between τ_{SO} and τ_p exhibits a significantly smaller slope. The changes are mainly due to a slower τ_{SO} growth for negative V_g, because the Hall signals are linear over the whole V_g range [18,45]. By introducing a coefficient $r = H_{R2}^{(1)}/H_{R2}^{(3)}$ [47], we have also fitted the V_g-dependent WAL-to-WL crossovers in Fig. 4(b) with the original ILP theory, which further confirms the dominant role of $H_{R2}^{(3)}$ with $r < 1/3$. Such a finding also explains the DFT-calculated hidden-spin textures in Fig. 1(c), which conspicuously deviate from the helical spin-momentum locking structure of **k**-linear Rashba SOC.

III. NONLOCAL TRANSPORT

After elucidating the mechanism of unlocking hidden R2-Rashba spins, it is natural to ask how long these locally generated effective spins can diffuse along the working channel, a critical parameter for spintronics. To our delight, we have observed robust nonlocal transport behavior in $SnSe_2$. As shown in Fig. 4(e) for a representative device, nonlocal (NL) device S2, the SOC-scattering-generated spins can readily reach a spin diffusion length λ_s exceeding 5 μm. Unlike conventional inversion-asymmetric spin systems [1], fast momentum scattering in $SnSe_2$ protects the effective spin polarizations by motional narrowing rather than to flip the spin polarizations. For such a unique DP spin relaxation system, nonlocal signals R_{NL}/ρ have the following

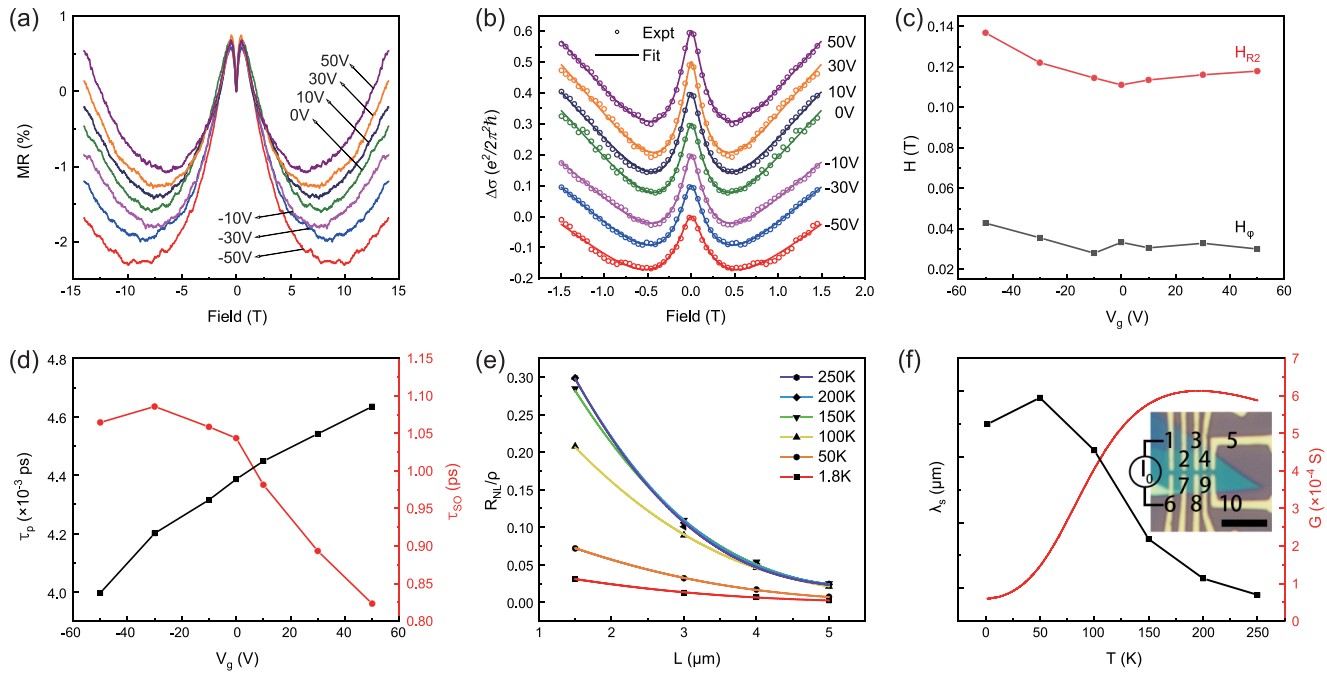

FIG. 4. Gate-tunable hidden-spin activations and nonlocal measurements. (a) The V_g-dependent MR curves of FET device SS3 at 2 K. (b) The corresponding MC characteristics fitted by the ILP theory. Note that the fitting is limited to ± 1.5 T, beyond which the conventional quadratic MR growth gradually takes over. (c) Gate-tunable H_φ and H_{R2}, extracted from the ILP fitting. (d) τ_{SO} deduced from the fitting, showing the V_g-polarity dependence of the inverse τ_{SO}-τ_p relation. (e) T-dependent nonlocal transport in NL device S2 with a channel width of $W = 0.5$ μm. R_{NL}/ρ shows the characteristic exponential decrease as a function of diffusion channel length. (f) T-dependent λ_s deduced from the Eq. (2) fitting. Note that there is no correlation between λ_s and G. Inset: Optical image of NL device S2 with a scale bar of 5 μm. Electrodes 1 and 6 are used for current injection.

dependencies:

$$R_{NL}/\rho \sim \left(\frac{\hbar\tau_p}{m^*\lambda_s^2}\right)^2 \frac{W}{\lambda_s} \mathrm{Re}(e^{ik|L|}), \tag{2}$$

where L and W are the channel length and width, respectively, and k is a complex wave vector proportional to $1/\lambda_s$ [48]. By fitting the experimental data to Eq. (2), we have extracted T-dependent λ_s in Fig. 4(f). We have also measured the electrical conductance G for different nonlocal channel lengths. The results consistently show an opposite T dependence in G compared with λ_s, evincing that there is no cross talk between these two signals.

IV. CONCLUSION

In summary, we have demonstrated that by introducing Se vacancies, the resulting SOC scattering can effectively create spin polarizations with finite spin relaxation time in multilayer $SnSe_2$. The surprising finding is rooted in the motion-narrowing random walks of precessing conduction electrons in the strong built-in R2-Rashba fields, when the chiral symmetry between the two Se sublattices is broken by vacancy-site SOC scattering. The leading contributions of cubic Rashba SOC in the ILP theory analyses suggest that our current understanding of the hidden spins may require further exploration. The robust nonlocal transport of the SOC-scattering-activated spins and unique gate tunability for τ_{SO} may open a playground for exploring unconventional spin physics and device prototypes. It is noteworthy that the aforementioned spin polarization mechanism emerges from sublattice chiral symmetry breaking, which is generally applicable for $1T$-TMDC systems. Indeed, we have noticed that defect-induced WAL has also been observed in $1T$-$PtSe_2$ [9,49,50].

ACKNOWLEDGMENTS

This work is supported by the Zhejiang Provincial Natural Science Foundation (Grant No. D19A040001), the National Science Foundation of China (Grant No. 11790313), and the National Key R&D Program of the MOST of China (Grant No. 2017YFA0303002). Y.Z. acknowledges support from the Users with Excellence Project of Hefei Science Center CAS, 2021HSC-UE007.

[1] R. Winkler, in *Spin-Orbit Coupling Effects in Two-Dimensional Electron and Hole Systems* (Springer, Berlin, 2003).

[2] A. Manchon, H. C. Koo, J. Nitta, S. M. Frolov, and R. A. Duine, Nat. Mater. **14**, 871 (2015).

[3] G. F. Dresselhaus, Phys. Rev. **100**, 580 (1955).

[4] E. I. Rashba, Sov. Phys. Solid State **2**, 1109 (1960).

[5] X. Zhang, Q. Liu, J. Luo, A. J. Freeman, and A. Zunger, Nat. Phys. **10**, 387 (2014).

[6] K. Gotlieb, C.-Y. Lin, M. Serbyn, W. Zhang, C. L. Smallwood, C. Jozwiak, H. Eisaki, Z. Hussain, A. Vishwanath, and A. Lanzara, Science **362**, 1271 (2018).

[7] J. Železný, H. Gao, K. Výborný, J. Zemen, J. Mašek, A. Manchon, J. Wunderlich, J. Sinova, and T. Jungwirth, Phys. Rev. Lett. **113**, 157201 (2014).

[8] J. M. Riley, F. Mazzola, M. Dendzik, M. Michiardi, T. Takayama, L. Bawden, C. Granerød, M. Leandersson, T. Balasubramanian, M. Hoesch, T. K. Kim, H. Takagi, W. Meevasana, P. Hofmann, M. S. Bahramy, J. W. Wells, and P. D. C. King, Nat. Phys. **10**, 835 (2014).

[9] W. Yao, E. Wang, H. Huang, K. Deng, M. Yan, K. Zhang, K. Miyamoto, T. Okuda, L. Li, Y. Wang, H. Gao, C. Liu, W. Duan, and S. Zhou, Nat. Commun. **8**, 14216(2017).

[10] A. Shafique, A. Samad, and Y. Shin, Phys. Chem. Chem. Phys. **19**, 20677 (2017).

[11] X. Zhou, N. Zhou, C. Li, H. Song, Q. Zhang, X. Hu, L. Gan, H. Li, J. Lü, J. Luo, J. Xiong, and T. Zhai, 2D Mater. **4**, 025048 (2017).

[12] P. Tan, X. Chen, L. Wu, Y. Shang, W. Liu, J. Pan, and X. Xiong, Appl. Catalysis B: Environ. **202**, 326 (2017).

[13] S. Datta and B. Das, Appl. Phys. Lett. **56**, 665 (1990).

[14] I. Zutic, J. Fabian, and S. Das Sarma, Rev. Mod. Phys. **76**, 323 (2004).

[15] W. Han, R. K. Kawakami, M. Gmitra, and J. Fabian, Nat. Nanotechnol. **9**, 794 (2014).

[16] H. Schmidt, I. Yudhistira, L. Chu, A. H. Castro Neto, B. Özyilmaz, S. Adam, and G. Eda, Phys. Rev. Lett. **116**, 046803 (2016).

[17] Z. Wang, C. Fan, Z. Shen, C. Hua, Q. Hu, F. Sheng, Y. Lu, H. Fang, Z. Qiu, J. Lu, Z. Liu, W. Liu, Y. Huang, Z. Xu, D. W. Shen, and Y. Zheng, Nat. Commun. **9**, 47 (2018).

[18] See Supplemental Material at http://link.aps.org/supplemental/10.1103/PhysRevB.107.165419 for Raman and atomic force microscopy characterizations, DFT calculations of R2-Rashba hidden spins and electron doping by Se vacancies, and data fitting by the original Iordanskii–Lyanda-Geller–Pikus (ILP) theory, etc.

[19] G. Kresse and J. Hafner, Phys. Rev. B **47**, 558 (1993).

[20] G. Kresse and J. Furthmüller, Phys. Rev. B **54**, 11169 (1996).

[21] J. P. Perdew, K. Burke, and M. Ernzerhof, Phys. Rev. Lett. **77**, 3865 (1996).

[22] G. Kresse and D. Joubert, Phys. Rev. B **59**, 1758 (1999).

[23] W. Ku, T. Berlijn, and C-C. Lee, Phys. Rev. Lett. **104**, 216401 (2010).

[24] Note that there is an intermixed growth of SnSe and $SnSe_2$ during crystal syntheses. The absence of exfoliated SnSe flakes is likely due to the formation of unique interlayer point dislocations within the SnSe domains (see Ref. [17]), since the elastic moduli of the two compounds are comparable.

[25] M. I. Dyakonov, in *Spin Physics in Semiconductors* (Springer, Berlin, 2008).

[26] J. Balakrishnan, G. K. W. Koon, M. Jaiswal, A. H. Castro Neto, and B. Özyilmaz, Nat. Phys. **9**, 284 (2013).

[27] M. Liu, J. Zhang, C.-Z. Chang, Z. Zhang, X. Feng, K. Li, K. He, L.-l. Wang, X. Chen, X. Dai, Z. Fang, Q.-K. Xue, X. Ma, and Y. Wang, Phys. Rev. Lett. **108**, 036805 (2012).

[28] Z. Wang, Y. Zheng, Z. Shen, Y. H. Lu, H. Fang, F. Sheng, Y. Zhou, X. Yang, Y. Li, C. Feng, and Z. A. Xu, Phys. Rev. B **93**, 121112(R) (2016).

[29] J. Chen, H. J. Qin, F. Yang, J. Liu, T. Guan, F. M. Qu, G. H. Zhang, J. R. Shi, X. C. Xie, C. L. Yang, K. H. Wu, Y. Q. Li, and L. Lu, Phys. Rev. Lett. **105**, 176602 (2010).

[30] H.-Z. Lu and S.-Q. Shen, Phys. Rev. B **84**, 125138 (2011).

[31] I. T. Rosen, I. Yudhistira, G. Sharma, M. Salehi, M. A. Kastner, S. Oh, S. Adam, and D. Goldhaber-Gordon, Phys. Rev. B **99**, 201101(R) (2019).

[32] V. Sazgari, G. Sullivan, and I. I. Kaya, Phys. Rev. B **101**, 155302 (2020).

[33] H.-Z. Lu, J. Shi, and S.-Q. Shen, Phys. Rev. Lett. **107**, 076801 (2011).

[34] F. G. Pikus and G. E. Pikus, Phys. Rev. B **51**, 16928 (1995).

[35] H_φ is correlated to the phase coherence time τ_φ by the relation $\tau_\varphi = m^*/4\pi\hbar\mu n H_\varphi$. For quantum-interference-introduced conduction corrections, H_φ is more intuitive than τ_φ for modeling and analyzing the experiment results, and the former is used for discussions in this paper.

[36] M. I. D'yakonov and V. I. Perel', Sov. Phys. JETP **33**, 1053 (1971).

[37] W. Knap, C. Skierbiszewski, A. Zduniak, E. Litwin-Staszewska, D. Bertho, F. Kobbi, J. L. Robert, G. E. Pikus, F. G. Pikus, S. V. Iordanskii, V. Mosser, K. Zekentes, and Yu. B. Lyanda-Geller, Phys. Rev. B **53**, 3912 (1996).

[38] R. J. Elliott, Phys. Rev. **96**, 266 (1954).

[39] Y. Yafet, in *g Factors and Spin-Lattice Relaxation of Conduction Electrons* (Academic, New York, 1963).

[40] S. Hikami, A. I. Larkin, and Y. Nagaoka, Prog. Theor. Phys. **63**, 707 (1980).

[41] The m^* used here to calculate τ_p is deduced from the density functional theory calculations, because the Shubnikov–de Haas oscillations are too weak to extract convincing information.

[42] R. Moriya, K. Sawano, Y. Hoshi, S. Masubuchi, Y. Shiraki, A. Wild, C. Neumann, G. Abstreiter, D. Bougeard, T. Koga, and T. Machida, Phys. Rev. Lett. **113**, 086601 (2014).

[43] W. Lin, L. Li, F. Doğan, C. Li, H. Rotella, X. Yu, B. Zhang, Y. Li, W. S. Lew, S. Wang, W. Prellier, S. J. Pennycook, J. Chen, Z. Zhong, A. Manchon, and T. Wu, Nat. Commun. **10**, 3052 (2019).

[44] J. Zeng, S.-J. Liang, A. Gao, Y. Wang, C. Pan, C. Wu, E. Liu, L. Zhang, T. Cao, X. Liu, Y. Fu, Y. Wang, K. Watanabe, T. Taniguchi, H. Lu, and F. Miao, Phys. Rev. B **98**, 125414 (2018).

[45] The divergent V_g-polarity dependence of τ_{SO} can be understood by the screening of the positive-V_g electric field due to the accumulation of additional holes at the interfacial regime, while the negative-V_g electric field is able to penetrate more $SnSe_2$ layers by the depletion mechanism (see Ref. [46]).

[46] Y. Liu, Z. Qiu, A. Carvalho, Y. Bao, H. Xu, S. J. R. Tan, W. Liu, A. H. Castro Neto, K. P. Loh, and J. Lu, Nano Lett. **17**, 1970 (2017).

[47] C. Niu, G. Qiu, Y. Wang, Z. Zhang, M. Si, W. Wu, and P. D. Ye, Phys. Rev. B **101**, 205414 (2020).

[48] D. A. Abanin, A. V. Shytov, L. S. Levitov, and B. I. Halperin, Phys. Rev. B **79**, 035304 (2009).

[49] Z. Li, Y. Zeng, J. Zhang, M. Zhou, and W. Wu, Phys. Rev. B **98**, 165441 (2018).

[50] J. Jo, J. H. Kim, C. H. Kim, J. Lee, D. Choe, I. Oh, S. Lee, Z. Lee, H. Jin, and J.-W. Yoo, Nat. Commun. **13**, 2759 (2022).